Space Weather®

RESEARCH ARTICLE
10.1029/2025SW004675

Driving Dynamical Inner-Heliosphere Models With In Situ Solar Wind Observations

M. J. Owens[1], L. A. Barnard[1], H. Turner[1], D. Gyeltshen[1], N. Edward-Inatimi[1], J. O'Donoghue[1], M. Lockwood[1], S. Watson[1], M. Rutala[2], C. M. Jackman[2], and P. Riley[3]

[1]Department of Meteorology, University of Reading, Reading, UK, [2]Astronomy & Astrophysics Section, School of Cosmic Physics, Dublin Institute for Advanced Studies, DIAS Dunsink Observatory, Dublin, Ireland, [3]Predictive Science, San Diego, CA, USA

Key Points:

- Inner-boundary conditions to solar wind models at 0.1 AU can be produced from in situ observations, typically at 1 AU
- We describe and test methods to account for transient structures, solar wind acceleration and stream interactions between 0.1 and 1 AU
- This enables quick and accurate reconstruction of inner-heliosphere structure without the need for magnetograms

Correspondence to:
M. J. Owens,
m.j.owens@reading.ac.uk

Citation:
Owens, M. J., Barnard, L. A., Turner, H., Gyeltshen, D., Edward-Inatimi, N., O'Donoghue, J., et al. (2026). Driving dynamical inner-heliosphere models with in situ solar wind observations. *Space Weather*, *24*, e2025SW004675. https://doi.org/10.1029/2025SW004675

Received 13 AUG 2025
Accepted 10 DEC 2025

Author Contributions:
Conceptualization: M. J. Owens, J. O'Donoghue, M. Rutala, C. M. Jackman
Data curation: P. Riley
Funding acquisition: M. J. Owens
Methodology: M. J. Owens, L. A. Barnard, H. Turner, D. Gyeltshen, N. Edward-Inatimi, M. Rutala
Software: M. J. Owens, L. A. Barnard
Visualization: M. J. Owens
Writing – original draft: M. J. Owens
Writing – review & editing: M. J. Owens, L. A. Barnard, H. Turner, D. Gyeltshen, N. Edward-Inatimi, J. O'Donoghue, M. Lockwood, S. Watson, M. Rutala, C. M. Jackman, P. Riley

Abstract Accurately reconstructing the solar wind throughout the inner heliosphere is essential for understanding solar–terrestrial interactions and improving space-weather forecasts. Conventional reconstruction methods rely on photospheric magnetic field observations and coronal models to estimate solar wind conditions near the Sun, typically at 0.1 AU. This introduces substantial uncertainty in the background flow used by heliospheric models through which coronal mass ejections (CMEs) propagate. Here we present a new approach that instead derives the inner-boundary conditions directly from in situ solar wind observations, typically obtained near 1 AU. These observations are ballistically backmapped to 0.1 AU while accounting for both solar wind acceleration and solar rotation, and then corrected for stream-interaction effects using a convolutional neural network trained on synthetic model data. The resulting 0.1 AU boundary conditions are used to drive the Heliospheric Upwind eXtropolation with time dependence (HUXt) model. Applied to the highly geoeffective May 2024 CME interval, this method reproduces solar wind conditions at Earth and at *Solar Orbiter*—on the far side of the Sun—with speed errors reduced by around 50% relative to traditional coronal-model approaches. Although this represents a post-event reconstruction rather than an operational forecast, the approach provides a fast, accurate, and magnetogram-independent means of reconstructing the inner heliosphere, paving the way for improved CME analyses and future forecasting applications.

Plain Language Summary Space weather is variability in the Sun's magnetic field that affects the space environment around Earth and other planets. The most severe space-weather disturbances occur when large eruptions of solar material and magnetic field, called Coronal Mass Ejections (CMEs), travel through the solar wind and impact Earth's own magnetic field. Predicting the arrival and strength of CMEs requires knowledge of the background solar wind conditions through which CMEs move. In this study, we show how direct measurements of the solar wind near Earth can be used to estimate conditions much closer to the Sun. This is achieved by tracing the observed solar wind back toward the Sun, while accounting for how it accelerates and interacts with faster or slower streams. We then use a computer model to simulate how these conditions evolve back out through the solar system. In this way, we successfully reproduce the conditions of the strong solar storms of May 2024. This demonstrates that near-Earth measurements can be used to provide a simple and accurate way to reconstruct the solar wind throughout the inner solar system. This is an important step toward improving space-weather forecasts in the future.

1. Introduction and Background

Accurate reconstruction of the solar wind structure between the Sun and the Earth is required for both space-weather forecasting and better understanding of the physics of the Sun-Earth system. In particular, ambient solar wind conditions influence the arrival of coronal mass ejections (CMEs) in near-Earth space (Case et al., 2008; Wu et al., 2024). At present, ambient solar wind reconstructions are limited by uncertainty in the near-Sun solar wind conditions that serve as the inner boundary to heliospheric models (Macneil et al., 2022; Yardley et al., 2024).

1.1. Overview of Existing Solar Wind Reconstruction Approaches

There are a number of different approaches to reconstructing the properties of the solar wind at different locations in the heliosphere, as shown schematically in Figure 1. Each of these has different strengths and weaknesses which makes them more or less suitable for different applications.

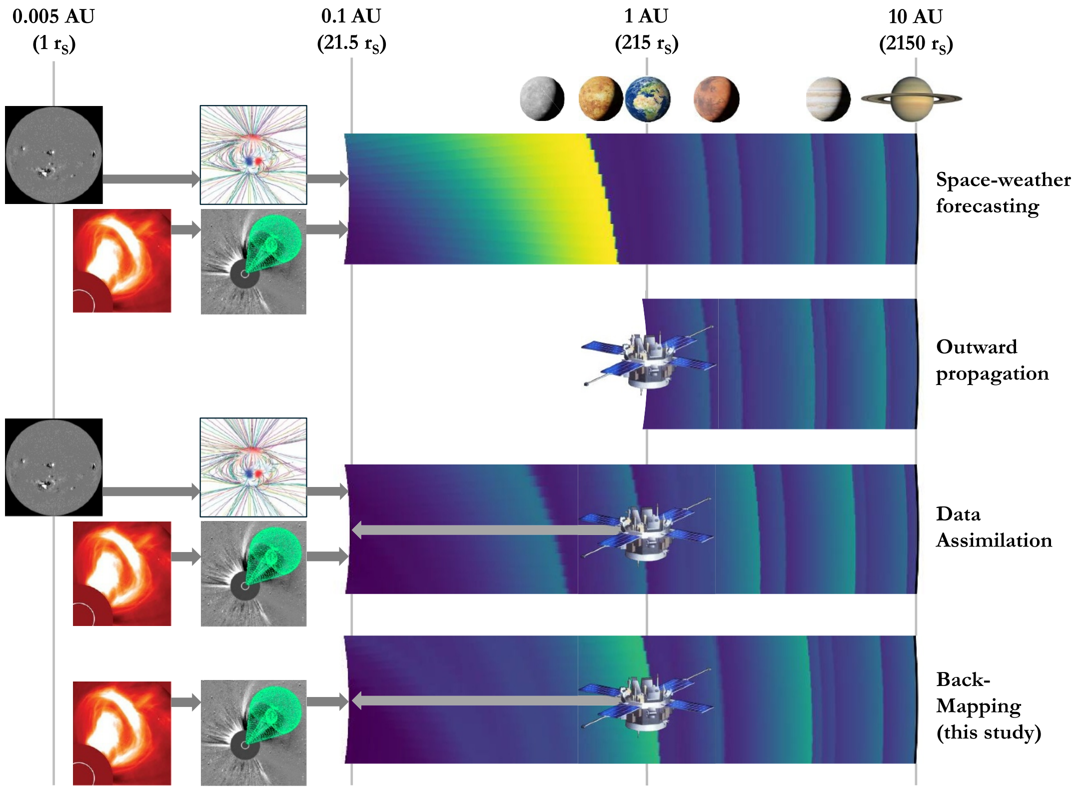

Figure 1. Schematic of different solar wind forecasting frameworks. Top row: The standard space-weather forecasting method, wherein the observed photospheric magnetic field is used to constrain a coronal model that provides an estimate of the ambient solar wind properties at 0.1 AU. Coronagraph observations of coronal mass ejections (CMEs) are used to derive cone-model parameters that are then added to the ambient wind as time-dependent perturbations at 0.1 AU. These are the combined inner-boundary conditions for a solar wind model which begins at 0.1 AU. Second row: The solar wind observed in situ, typically at 1 AU, can be used directly as the inner-boundary condition for a solar wind model which begins at 1 AU. Third row: in situ solar wind observations can be used with a data-assimilation scheme to update the ambient coronal-model estimates at 0.1 AU. Cone-model CMEs can be inserted at 0.1 AU, as in the space-weather forecasting approach. Bottom row: The methodology developed in this study, wherein in situ solar wind observations are back-mapped to 0.1 AU and used as inner-boundary conditions to the solar wind model. Again, cone-model CMEs can be inserted at 0.1 AU.

The top row in Figure 1 shows the standard method for forecasting solar wind conditions, particularly CMEs, in near-Earth space a few days into the future. This same approach is also frequently used for post-hoc reconstruction of inner-heliosphere conditions. The observed photospheric magnetic field is used to constrain a model of the coronal magnetic field (e.g., Arge et al., 2003; Riley et al., 2001; van der Holst et al., 2014), which is used as the basis for an estimate of the ambient solar wind conditions at 0.1 AU, typically through empirical relations to the coronal field structure. Coronagraph images of CMEs are used with a "cone model" to characterize a time-dependent perturbation at 0.1 AU (e.g., Palmerio et al., 2023; Zhao, 2008). These two inputs are combined to produce inner-boundary conditions for a solar wind model (e.g., Merkin et al., 2016; M. Owens et al., 2020; Pomoell & Poedts, 2018; Riley et al., 2001; Toth et al., 2005), which dynamically propagates conditions throughout the heliosphere.

A typical example of this space-weather approach is shown in Figure 2, for a 40-day interval containing the highly geoeffective May 2024 CMEs (e.g., Hayakawa et al., 2025; Lockwood et al., 2025). The model results were produced using the Global Oscillations Network Group (Harvey et al., 1996) daily-updated magnetogram for 2024-5-10, with the Wang-Sheeley-Arge coronal model (Arge et al., 2003). This produces an estimate of solar wind speed at 0.1 AU which serves as the inner-boundary condition to the Heliospheric Upwind eXtropolation with time dependence (HUXt) solar wind model (M. Owens et al., 2020; Barnard & Owens, 2022, see also Section 2.2). This gives the estimate of the ambient solar wind in the ecliptic plane shown in the top panels, with the solid red line in the bottom panel showing the time series at Earth. Cone CME properties estimated from coronagraph observations as part of the DONKI database (described further in Section 2), are added to the

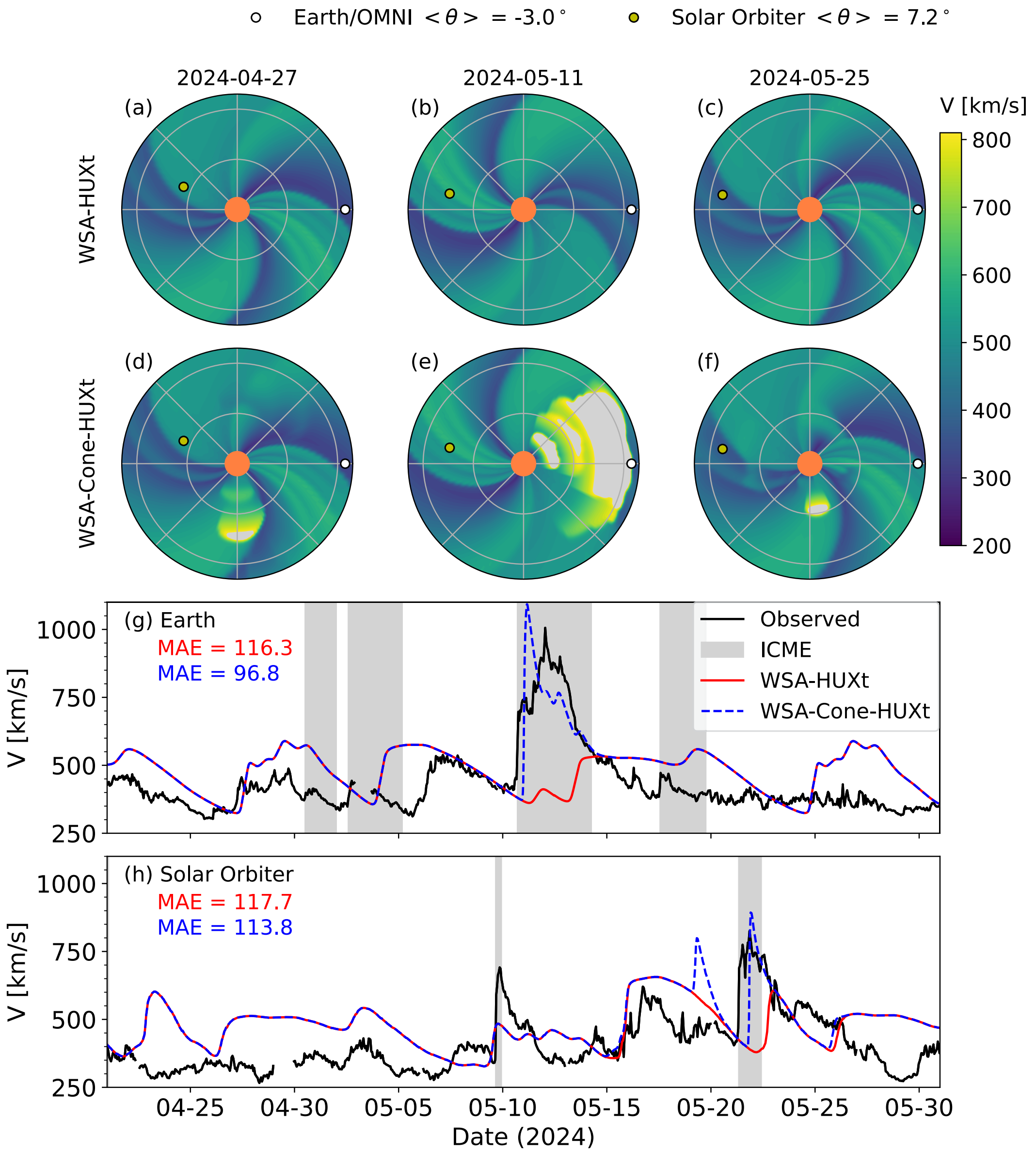

Figure 2. An example of solar wind reconstruction using the space-weather approach. The WSA coronal model solution to the 2024-5-10 GONG magnetogram and cone coronal mass ejections (CMEs) from coronagraph observations are used to provide the inner-boundary conditions to the HUXt solar wind model. The period around the May 2024 storms is shown. Panels (a) to (c) show the ambient solar wind speed (i.e., WSA-HUXt without cone CMEs) in the ecliptic plane at three times; before, during and after the storms. Earth is shown as a white circle, *Solar Orbiter* as a yellow circle. Panels (d) to (f) show the same times, but for WSA-Cone-HUXt. (g) Time series of solar wind speed observed (black) in near-Earth space, with times of observed interplanetary CMEs shown as gray-shaded areas. The ambient WSA-HUXt solution is shown in red, with WSA-Cone-HUXt shown by the blue-dashed line. (h) Same as g, but at the location of *Solar Orbiter*.

ambient solution, yielding the WSA-Cone-HUXt solar wind speed estimate shown by the blue-dashed line. CMEs that arrived in near-Earth space—interplanetary CMEs (ICMEs)—are identified using the updated Richardson and Cane (2010) catalog and are shown by the gray-shaded intervals. There are clearly Earth-directed cone CMEs that are not subsequently seen at Earth, and ICMEs at Earth that were not predicted on the basis of coronagraph observations. This is not uncommon; extracting three-dimensional CME information from coronagraph images is challenging. However, this study focuses primarily on the ambient wind, outside of those intervals; this "space-weather" approach produces approximately the correct number of fast/slow streams, but there are significant timing (~days) and magnitude (~100 km s^{-1}) errors compared with the observed near-Earth solar wind, shown by the solid black line. These ambient solar wind errors will reduce the accuracy of ICME arrival time and speed estimates, even if the cone-CME parameters are perfect (Case et al., 2008; Wu et al., 2024).

The advantages of this space-weather approach are that it can treat the solar wind as a fully three-dimensional flow, allowing the latitudinal positions of different target objects (e.g., Earth and the *Solar Orbiter* spacecraft) to be accurately accommodated. It also correctly represents ambient solar wind structure as approximately co-rotating with the Sun, and CMEs as time-dependent, transient structures (though the inner-boundary conditions may be inaccurate). The primary disadvantage of this approach is that the photospheric magnetic field only contains very indirect information about the solar wind flow at 0.1 AU (Riley et al., 2015; Wang & Sheeley, 1990) and that the estimated solar wind conditions are highly sensitive to both the choice of coronal model and precisely how the photospheric observations are processed (e.g., Heinemann et al., 2025; Majumdar et al., 2025).

When estimating the solar wind at locations outside Earth orbit, solar wind models can instead be initialized with direct, in situ solar wind observations, as shown by the second row in Figure 1. The simplest approach to this is to use a one-dimensional model to propagate the observed solar wind, typically from near-Earth space, out to the heliocentric distance of a target object of interest, such as Mars or Jupiter (Tao et al., 2005). If the target and input in situ observations are in radial alignment, this approach should work extremely well. However, with increasing angular separation (with respect to the Sun) of input and target, it is necessary to make a number of additional assumptions and approximations. A one-dimensional solution can be rotated to the target longitude, assuming all the observed solar wind structures perfectly co-rotate with the Sun. Alternatively, two-dimensional models can be used which explicitly allow for the longitudinal difference, but some form of corotation assumption is still required to produce an estimate of solar wind conditions at all longitudes from a single-point observation (Keebler, 2021). While directly using accurate solar wind observations, this approach comes with a number of limitations. Firstly, solar wind estimates can only be made downstream of the input observation and are limited to latitudes of the observing spacecraft. Secondly, any transient ICMEs in the input solar wind observations, unless actively removed, will be treated as corotating structures and potentially produce false fast streams at other longitudes. Thirdly, there is the converse issue: CMEs that did not pass over the observing spacecraft cannot easily be incorporated, as information about CMEs from remote sensing observations is only routinely available close to the Sun, typically at 0.1 AU.

The strengths of the space-weather approach can be combined with the accurate information contained in solar wind observations by the use of data assimilation (DA), which seeks to combine model and observation, accounting for the uncertainty in both. Initial attempts at solar wind DA suffered one of the same problems as the outward-propagation methods: Reconstruction of solar wind conditions was only improved downstream of the assimilated observation location (Lang et al., 2017). More recently, methodologies have been developed to persistently update the solar wind model inner-boundary conditions at 0.1 AU on the basis of in situ observations at 1 AU (Lang & Owens, 2019). This has been shown to improve reconstruction and forecasting of ambient solar wind in near-Earth space (Lang et al., 2021; Turner et al., 2023). However, this improvement is limited to a small latitudinal range around the observation location (Turner et al., 2021; Watson et al., 2025). As the solar-model inner boundary remains at 0.1 AU, this approach can still use cone-CME estimates to properly incorporate transient solar wind structures resulting from CMEs.

Scientifically, the DA approach is the best currently available for both reconstructing and forecasting the ambient solar wind, and for subsequently including CMEs. In practice, however, there are non-trivial barriers to its widespread use by the scientific community. It requires availability of magnetograms for the period of interest. It then requires access to, and ability to run, a coronal model that has been tuned for use with the chosen photospheric observatory; many coronal models are not open source or simple to run, though facilities like the Community Coordinated Modeling Center (https://ccmc.gsfc.nasa.gov/) dramatically reduce the barrier to entry in this regard. Finally, a DA scheme must be run (a solar wind DA implementation is available here: https://github.com/University-of-Reading-Space-Science/BRaVDA). Putting aside these technical hurdles, the output of the DA will be sensitive to the choice of magnetogram and coronal model, as well as the DA methodology itself (Arnal & Groth, 2024). Furthermore, the current solar wind DA implementation (Lang & Owens, 2019) is time stationary. This means independent assimilation runs are required for each update of the photospheric magnetic field. For long solar wind reconstructions—of months or years, that are often required for the outer planets—this can mean running many hundreds of assimilation windows, which is both computationally expensive and logistically challenging in terms of compiling the inputs and outputs.

1.2. A New Approach

In this study, we propose a simple alternative to solar wind DA, which still retains many of its advantages. We show how in situ solar wind observations from 1 AU can be "backmapped" to 0.1 AU. Doing so requires accounting for both pressure-driven solar wind acceleration and stream interactions between 0.1 and 1 AU. We show how this can be achieved, yielding inner-boundary conditions for dynamical solar wind models without the need for photospheric observations or a coronal model. This allows the method to be used when magnetograms are not available, and removes the sometimes prohibitive requirement for running both a coronal model and a DA scheme. It also makes the computing requirements and logistics of long intervals of solar wind reconstructions substantially easier.

Section 2 details the data and models used in the study, Section 3 outlines the methodology. Section 4 shows the results of applying the new method to the same May 2024 interval used to illustrate the space-weather approach in Figure 2. Section 5 summarizes and discusses the implications of these results and avenues for future research.

2. Data and Models

2.1. Data

Near-Earth solar wind observations are provided by the OMNI (King & Papitashvili, 2005) data set, available from https://omniweb.gsfc.nasa.gov/. We use the 1-hr data. Additionally, solar wind speed measurements at *Solar Orbiter* (Muller et al., 2013) are provided by the Solar Wind Analyzer suite of instruments (Owen et al., 2020), available from https://cdaweb.gsfc.nasa.gov/. Data are averaged to 1 hr resolution. We here focus on solar wind speed, V.

In order to identify intervals of solar wind resulting from the passage of transient ICMEs over the observing spacecraft, we use two ICME catalogs. For near-Earth space (and hence the OMNI data set), we use the Richardson and Cane (2010) ICME catalog, available from https://izw1.caltech.edu/ACE/ASC/DATA/level3/icmetable2.htm. At *Solar Orbiter* we use the Möstl et al. (2017) catalog, available at https://helioforecast.space/icmecat.

In order to reintroduce transient structures associated with CMEs into the solar wind model, we require estimates of CME direction, speed, width and timing at 0.1 AU. This data is taken from the DONKI database (https://ccmc.gsfc.nasa.gov/tools/DONKI/). The cone-CME parameters provided in DONKI are primarily from the Moon-to-Mars (M2M) Space Weather Analysis Office, from analysis of available coronagraph data.

2.2. The HUXt Solar Wind Model

The efficacy of the backmapping process is tested using the Heliospheric Upwind eXtrapolation with time dependence (HUXt) model (M. Owens et al., 2020; Barnard & Owens, 2022). HUXt is a dynamical model that approximates the solar wind as a 1-dimensional, incompressible, hydrodynamic flow. It explicitly allows for continued acceleration of the solar wind flow between 0.1 and 1 AU in a manner consistent with polytropic magnetohydrodynamics, using a ratio of specific heats $\gamma = 5/3$ (see also Riley & Lionello, 2011, and Section 3.3). Solar wind flows also accelerate and decelerate through stream interaction. HUXt has been shown to reproduce solar wind speeds throughout the model domain from 0.1 to 1 AU in very close agreement (to within 5%) with 3-dimensional magnetohydrodynamic model for the same boundary conditions (M. Owens et al., 2020). This includes both steady-state solar wind and transient speed pulses associated with CMEs.

3. Methods

There are a number of distinct steps in producing estimates of solar wind conditions at 0.1 AU from 1-AU observations. These are shown schematically in Figure 3 and detailed in the remainder of this Section. Note that these steps are modular, and future developments in any of these areas can be easily incorporated into this general framework.

3.1. Removal of Transient ICMEs at 1 AU

In order to separate transient ICMEs from the quasi-steady-state ambient solar wind, we remove all solar wind values between 0.1 days prior to the ICME shock front and 1-day after the ICME trailing edge. In general, the

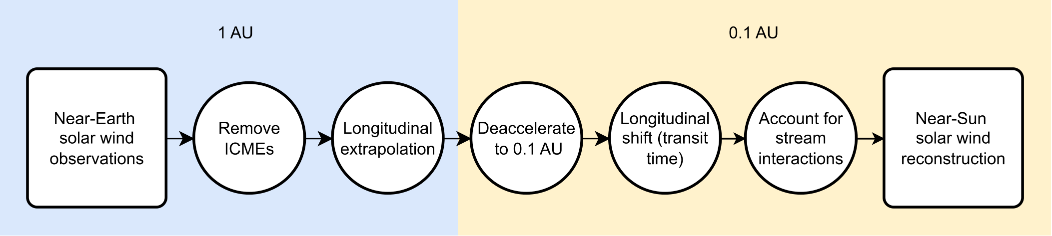

Figure 3. A schematic of the steps for backmapping 1-AU observations to 0.1 AU, as used in this study. The method underpinning each step is outlined in Section 3.

leading oedge of an IMCE is more clearly defined than the trailing edge. While these values are somewhat arbitrary, they allow for small uncertainty in the ICME start time and the continued disturbance of the ambient solar wind behind a fast ICME. Changing these values by ±100% does not significantly affect the results presented, but subsequent work will investigate the optimum values in a more statistical sense. The resulting gaps in the OMNI time series are filled with simple linear interpolation between the ambient wind ahead and behind. More sophisticated methods are being tested to fill the datagaps produced by removing ICMEs. These include using an analog ensemble to fill gaps with the most appropriate historical data (M. J. Owens et al., 2017; Riley et al., 2017), or training a Gaussian Process model to provide a number of statistically appropriate realizations of the missing data. The modular framework and codebase presented here means that these techniques can be easily integrated in the future, after they have been properly evaluated.

3.2. Providing Longitudinal Coverage at 1 AU

One of the challenges of driving solar wind models with in situ observations is that at any given time, only V at a single longitude (and latitude) is known. In order to completely specify the two-dimensional solar wind structure at Earth's current heliographic latitude, it is necessary to make further assumptions about the time-evolution of the ambient solar wind structure. A common assumption for solar wind forecasting is that the solar wind structure is fixed in time and corotates with the Sun. Thus V at a given Carrington longitude is equal to the last V observation at the same longitude; the solar wind structure is corotated back in time. When using near-Earth solar wind observations to predict future solar wind, this means assuming V tomorrow is equal to that observed ≈27-day previously, producing a forecast tool that is surprisingly effective (e.g., Kohutova et al., 2016; M. J. Owens et al., 2013).

Corotating forward in time to the next observation at a given longitude is obviously not possible for forecasting. But for reconstruction purposes it is an equally valid assumption. Corotation forward and backward in time produce identical longitudinal profiles of solar wind at 1 AU, but with a 27.27-day offset. These two corotation approaches can be combined by taking a time-weighted average of the previous and next observations of V at a given longitude (Keebler, 2021; M. J. Owens & Nichols, 2021). As will be shown later, this has the advantage of removing the discontinuous change in solar wind properties every 27 days as new observations are introduced. But it can "smear out" features. In particular, if a fast stream shifts slightly in Carrington longitude between consecutive Carrington rotations, the "corotation - both" approach will not produce any fast wind at any longitude, but instead intermediate speed wind over an extended longitude range (M. J. Owens & Nichols, 2021). To address this, discrete solar wind structures can be identified and matched between consecutive 27-day intervals and allowed to drift in longitude (M. J. Owens & Nichols, 2021). This "dynamic time warping (DTW)" approach avoids the "smearing out" issue.

One point to note here is that full longitudinal coverage can only be obtained over a duration shorter than the available OMNI data. In general, the input OMNI data needs to cover an extra 27.27 days before/after the required start/end of the interval to be reconstructed. This can be an issue for reconstructing very recent intervals (or actual forecasting). In those circumstances, only the corotation back in time method can be applied.

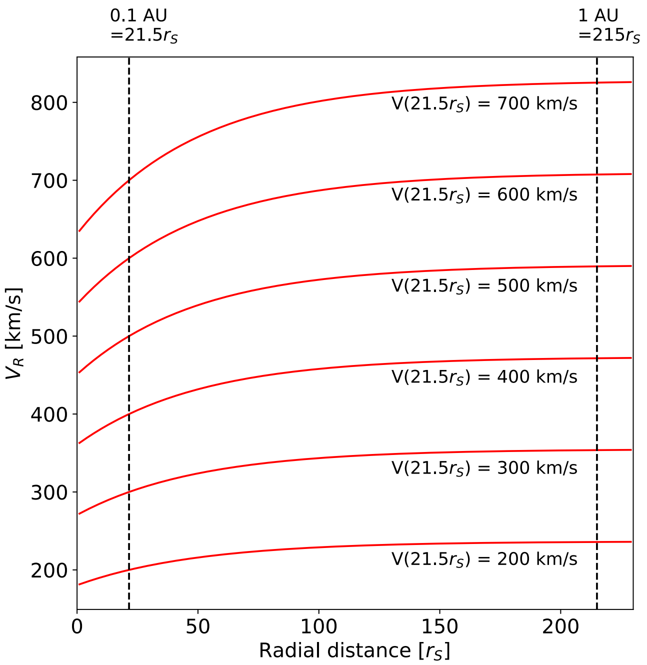

Figure 4. The solar wind acceleration profile used in the HUXt solar wind model for a range of initial speeds at the model inner boundary.

3.3. Solar Wind Acceleration

Solar wind parcels at each longitude at 1 AU are ballistically mapped back to 0.1 AU. It is necessary to account for continued solar wind acceleration during transit in order to avoid both an overestimation of the speed at 0.1 AU and in order to determine the correct transit time and hence shift in longitude due to solar rotation during transit.

The HUXt model assumes a solar wind acceleration profile consistent with pressure-driven expansion of the solar wind (Riley & Lionello, 2011). It has the form:

$$V(r) = V_0 + \alpha V_0 \left[1 - \exp\left(\frac{-(r - r_0)}{r_H} \right) \right], \tag{1}$$

where $V(r)$ is the solar wind speed at helioscentric distance r, V_0 is the speed at some reference height r_0, α is the acceleration factor and r_H is the scale height over which it applies. Riley and Lionello (2011) used $r_0 = 30\ \mathrm{R}_\odot$ and found $\alpha = 0.15$ and $r_H = 50\ \mathrm{R}_\odot$ produced a close match to 3D MHD results. This acceleration profile is shown for a range of V_0 in Figure 4. For all initial solar wind speeds, the speed asymptotes with increasing distance from the Sun, with the bulk of the acceleration occurring inside 100 $\mathrm{R}_\odot$.

Thus, a solar wind parcel with speed at 1 AU of V_{1AU} will have a speed at the reference height of $r_0 = 30\ \mathrm{R}_\odot$ given by:

$$V_0 = \frac{V_{1AU}}{1 + \alpha\left(1 - \exp \frac{r_0 - 1\ \mathrm{AU})}{r_H}\right)}. \tag{2}$$

The speed at r =0.1 AU is then given by:

$$V_{0.1\ \mathrm{AU}} = V_0 \left[1 + \alpha\left(1 - \exp \frac{r_0 - 1\ \mathrm{AU}}{r_H}\right)\right]. \tag{3}$$

3.4. Backmapping: Longitudinal Shift

The Sun continues to rotate during the transit of solar wind to 1 AU. In order to determine the transit time from 0.1 to 1 AU, τ, we integrate Equation 1 to get:

$$\tau = \frac{r_H}{V_0(1+\alpha)} \ln\left[.(1+\alpha)\exp\left(\frac{1\ \mathrm{AU} - 0.1\ \mathrm{AU}}{r_H} \right) - \alpha \right]. \tag{4}$$

Thus, solar rotation means that each solar wind parcel at a Carrington longitude at 1 AU of $\phi_{1\ \mathrm{AU}}$ maps to a Carrington longitude at 0.1 AU of:

$$\phi_{0.1\ \mathrm{AU}} = \phi_{1\ \mathrm{AU}} + 2\pi \frac{\tau}{T_{SY\ N}} \tag{5}$$

where $T_{SY\ N}$ is the solar synodic rotation period from Earth, approximately 27.27 days.

We assume that the ambient solar wind structure is not evolving over the time it takes the solar wind to propagate from 0.1 to 1 AU, typically 2–4 days (M. J. Owens et al., 2022). As solar wind parcels from multiple longitudes at 1 AU may map to similar longitudes at 0.1 AU, the solar wind parcels at 0.1 AU are no longer evenly spaced in longitude. We linearly interpolate speeds back onto the HUXt longitudinal grid of 128 regularly-spaced points to produce $V_{0.1AU}$ on a uniform longitudinal grid. This produces a first-order reconstruction, but neglects the effect of stream interactions between 0.1 and 1 AU.

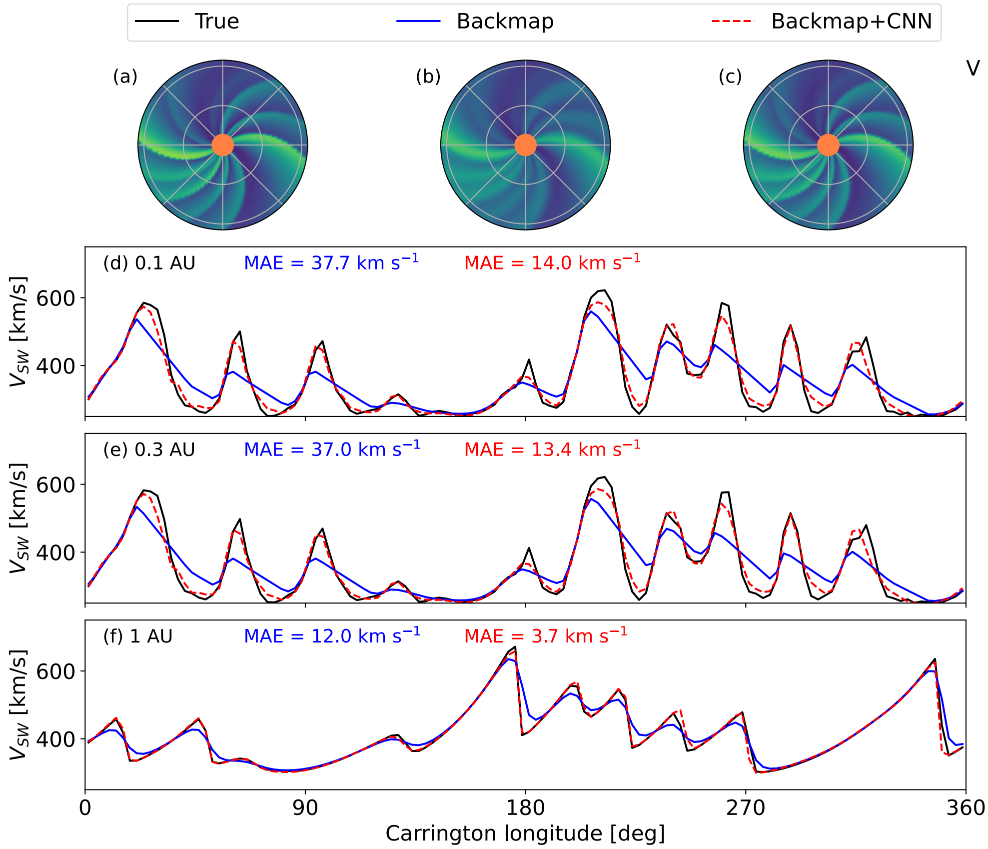

Figure 5. An example of ballistic backmapping using a synthetic solar wind solution. The HUXt solar wind speed in the solar-equatorial plane is shown for (a) true, (b) backmapped and (c) backmapped + convolutional neural network (CNN) inner boundary conditions. Speeds at three radial distances—(d) 0.1, (e) 0.3 and (f) 1 AU—are shown as a function of Carrington longitude (thus a time series of observations from a quasi-stationary spacecraft at a given distance would run from right to left). The black lines in all panels shows the true state generated from the 0.1 AU boundary condition used to drive the HUXt solar wind model out to 1 AU. The blue lines show the result of backmapping, allowing for acceleration, the synthetic 1-AU observations (from the true state), then running HUXt back out to 1 AU. The red lines show the backmapped solar wind additionally corrected for stream interactions by a CNN, which then is used to run HUXt out to 1 AU.

3.5. Backmapping: The Issue of Stream Interactions

It is difficult to assess the backmapping process with real data, as there are no simultaneous observations of solar wind at 1 and 0.1 AU with complete longitudinal coverage and at the same heliolatitude. Instead, we use synthetic data, where the true state of the system is known at all locations and all times. These synthetic solar wind observations are generated by a HUXt solar wind solution. The inner-boundary conditions at 0.1 AU need not be "real"; the aim is simply to test whether the resulting true state at 0.1 AU can be recovered from the synthetic 1 AU observations.

An example of a synthetic *V* profile at 0.1 AU is shown as the black line in Figure 5d. This was obtained from coronal model solutions generated using the HelioMAS model (Riley et al., 2001) obtained from https://www.predsci.com/mhdweb/home.php, as described further below. This speed profile at 0.1 AU is used as the inner-boundary condition to the HUXt model to generate the "true" solution in the solar-equatorial plane, shown Figure 5a. From this, we extract the true *V* profiles at 0.3 and 1 AU shown as black lines in Figures 5e and 5f, respectively. It can be seen that solar wind streams map to smaller Carrington longitudes at increasing heliocentric distance, consistent with a Parker spiral-like structure. Note that a time series for a stationary spacecraft would run from high to low Carrington longitude at a given distance. Thus the shift of features to smaller Carrington longitudes is a direct result of solar wind propagation time between different heliocentric distances.

At increasing heliocentric distance, the waveform of the solar wind streams becomes increasingly saw-tooth in shape (at least within 1 AU. At much greater heliocentric distances, stream interaction regions themselves begin to merge together Hanlon et al. (2004)). This is due to stream interactions between fast and slow wind; where fast wind catches up with slow wind, a sharp, shock-like, feature forms. Whereas a rarefaction region forms as fast wind runs ahead of slow wind (Pizzo, 1991). Within the space-weather modeling framework, the sharpness of the slow-to-fast wind transition is partly determined by the solar wind model numerics, and partly by the details of the coronal model that serves as input at 0.1 AU (Majumdar et al., 2025; Samara et al., 2024).

The true solution at 1 AU (black line in Figure 5f) is then treated as synthetic near-Earth observations. This is ballistically backmapped to 0.1 AU, allowing for solar wind acceleration and solar rotation, but not yet accounting for stream interactions. The result is shown as the blue line in Figure 5d. If the process was perfect, then the backmapped V profile would be identical to the true V profile (the black line). The general stream structure is well reproduced, but the speed gradient at one edge of each fast stream is systematically reduced. This is because of stream interactions between 0.1 and 1 AU. These result in the quasi-discontinuous speed increase at 1 AU formed at the fast/slow wind interface. Consequently, solar wind at similar times (and hence longitudes) at 1 AU can have a wide range of V and thus map to large range of longitudes at 0.1 AU.

The next step is to determine the effect of this imperfect backmapping on reconstructing the solar wind. We drive HUXt (forward in time) from 0.1 to AU using this imperfect backmapped solar wind as the inner boundary. It produces the solar wind speed in the solar-equatorial plane shown in Figure 5b. It can be seen that the solar wind stream interfaces are generally less sharp than the true values shown in the left-hand panel. We again extract the profiles at 0.3 and 1 AU, which are shown as the blue lines in Figures 5e and 5f, respectively. Comparing the true and backmapped HUXt solutions, the gradients at the leading edges of the stream interaction regions are greatly reduced. This is more apparent at 0.3 than 1 AU.

3.6. Backmapping: Accounting for Stream Interactions

The effects of stream interactions on the backmapping process are not easy to remove analytically, as they depend on the whole V profile as a function of longitude, rather than just a single value. But as the effect appears to be highly reproducible, it should be effectively addressed using a simple machine-learning algorithm. In order to train an algorithm we require a large data set of true profiles at 0.1 AU, and the equivalent backmapped profiles (i.e., multiple instances of the black and blue lines in Figure 5d).

Again, the training profiles do not need to be "real" instances of the Sun, though they should represent the structure in a statistical sense. To produce the training data set, we start with existing HelioMAS coronal solutions (https://www.predsci.com/mhdweb/home.php) to magnetograms for each Carrington rotation from 1861 to 2296 (i.e., March 1993 to April 2025). This is the interval of continuous data availability at the time of writing, spanning approximately three solar cycles. From each solution, we extract V as a function of Carrington longitude at heliolatitudes of -10, -5, 0 5 and 10°. The 5° separation is generally sufficient to produce a qualitatively different V profile, particularly at solar minimum (M. Owens et al., 2019; Turner et al., 2021). These 2180 V profiles are used as the "true" values at 0.1 AU. Each profile is next used as the inner-boundary condition for the HUXt model, which is run forward to 1 AU. The resulting HUXt longitudinal V profile at 1 AU is treated as synthetic spacecraft observations and is backmapped to 0.1 AU. These 2180 pairs of true and backmapped V profiles at 0.1 AU are then randomly assigned as either training data (4/5th of the data, 2180 pairs) or test data (1/5th of the data, 436 pairs).

We use a 1-dimensional convolutional neural network (CNN) to map the backmapped profiles onto the true profiles and ultimately correct them. The model, training and output data are all supplied as part of the code and data distribution (M. Owens, 2025). The CNN architecture was based on a standard approach using PyTorch (Paszke et al., 2019). It uses three convolutional layers. The first layer contains 32 filters with a kernel size of 5 and a rectified linear unit activation function. The second contains 64 filters, also with a kernel size of 5 and rectified linear unit activation. The final layer projects the features back to a single channel using 1 filter with a kernel size of 3. The CNN was trained on the training data using the mean-squared-error loss function. To avoid over fitting, training was performed on 50 randomly sampled subsets of the test data set.

Applying the CNN to the backmapped solar wind at 0.1 AU produces the red dashed line in Figure 5d, which is much closer to the true state. The implications of this, and testing on a wider data set, are discussed in Section 4.1.

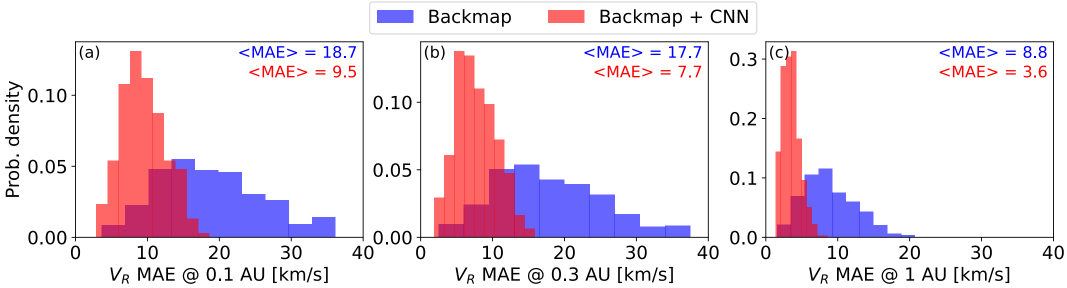

Figure 6. Mean absolute error (MAE) between the true solar wind speed and backmapped speed (blue), and backmapped speeds further modified by the convolutional neural network (red) for 436 solar wind speed longitudinal profiles in the test data set. Panels (a) to (c) show MAE at 0.1, 0.3 and 1 AU, respectively.

4. Results

In order to quantify the efficacy of the complete backmapping procedure, we take two complementary approaches. First, we examine the performance for a large database of synthetic 1-AU observations generated by the HUXt model. This has the advantage that the true state is known a priori. Second, we apply the same methods to observations during the May 2024 storms and compare the reconstruction with near-Earth and *Solar Orbiter* observations.

4.1. Testing With Synthetic Data

When the example synthetic profile shown in Figure 5 is backmapped to 0.1 AU without accounting for stream interactions, it results in a mean absolute error (MAE) compared to the true state of 37.7 km s^{-1}. Applying the CNN to account for stream interactions reduces this MAE to 15.1 km s^{-1}, approximately 60%. In particular, Figure 5d shows that the gradient of the solar wind speed at the transition from fast to slow wind is much closer to the true state. Using this "backmapped + CNN" V profile as the inner boundary for HUXt, the reconstructions at 0.3 and 1 AU are also in better agreement with the true state by around 60%–70% compared to backmapping alone. However, the improvement in absolute terms becomes less noticeable with increasing radial distance.

As described in Section 3.6, 436 V profiles generated from the HelioMAS model at 0.1 AU are excluded from training the CNN. These test data are all used as the inner boundary to the HUXt model, which is run out to 1 AU to generate 436 sets of synthetic spacecraft observations. These 436 synthetic 1-AU observations are backmapped to 0.1 AU, as detailed above. The HUXt model is then run back out to 1 AU from the backmapped values at 0.1 AU, both with and without the CNN applied. That is, we perform a total of 1,308 additional HUXt runs from 0.1 to 1 AU, each of duration 27 days.

Figure 6 shows the results across all 436 pairs of test V profiles. At the 0.1 AU inner boundary, the average MAE per speed profile from backmapping (including acceleration) is 18.7 km s^{-1}. After applying the CNN to the backmapped profile to account for stream interactions, this reduces to 9.5 km s^{-1}. At 0.3 AU, the average MAE for backmapping is 17.7 km s^{-1}, reduced to 7.7 km s^{-1} by the application of the CNN. Out at 1 AU, the percentage improvement provided by the CNN is similar, but the absolute error in the backmapping is low enough that the actual gain provided by the CNN is small.

Thus we may expect the addition of the CNN to the backmapping process to be particularly important for inner heliosphere studies, but less vital for outer heliosphere reconstructions. However, despite the modest improvement at 1 AU, the CNN may still be important for forecasting space-weather at Earth due to improved CME dynamics through the solar wind inside 0.3 AU. As the CNN is trivial to apply—both technically and in terms of computational overhead—the results in the remainder of the study are all based upon the backmapping + CNN approach.

4.2. Application to the May 2024 Observations

We now apply the complete method to real observations from the same May 2024 interval shown in Figure 7. The black line in the top panel shows the 1-hr OMNI data from near-Earth spacecraft (King & Papitashvili, 2005). The

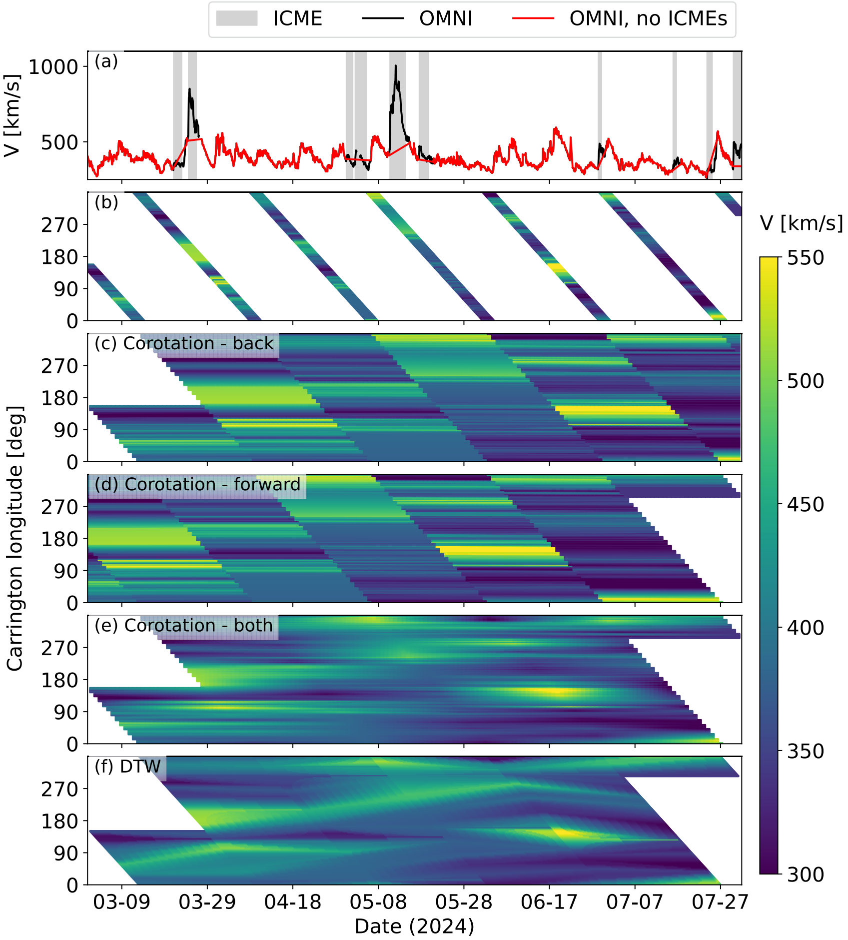

Figure 7. The solar wind speed, V, in near-Earth space around the time of the May 2024 geomagnetic storms. (a) Observed V from the OMNI data set as a function of time is shown as the black line. Times identified as transient interplanetary CMEs (ICMEs) are shown as gray-shaded regions. Removal of these ICMEs results in the red line. (b) The ICME-removed OMNI V shown as a function of Carrington longitude and time. (c) Reconstruction of V at all longitudes and time by assuming corotation back to the last observation at a given longitude. (d) Same as c, but assuming corotation forward in time. (e) Same as c, but taking a time-weighted average of corotation forward and backward in time. (f) Same as c, but using dynamic time warping.

gray-shaded regions show the intervals identified as ICMEs using the Richardson and Cane (2010) catalog. Removal of these ICMEs results in the red line.

We first consider the implications of not removing ICMEs before backmapping is applied. The solid red line in Figure 8d shows the result of mapping all OMNI observations—including ICMEs—back to 0.1 AU and then running the model back out to near-Earth space. As expected, the agreement at Earth is extremely good, both in the ambient solar wind and within ICMEs, shown by the gray-shaded regions. However, the right result is obtained for the wrong reasons. As can be seen in Panels a to c, backmapping the fast mid-May ICMEs at Earth to 0.1 AU creates a false corotating stream of very fast wind. At *Solar Orbiter*, on the far-side of the Sun from Earth, the model then predicts fast streams on 2025-4-25 and 2025-5-25, which are not observed (though there is a different fast ICME at *Solar Orbiter* on 2025-5-22). Removing ICMEs from the OMNI data before backmapping, as shown by the blue dashed line, removes these false fast streams at *Solar Orbiter*. Thus the remainder of this study focuses on backmapping the OMNI data with ICMEs removed. The ICMEs at Earth will later be reintroduced into the model as true transient structures on the basis of cone-model estimates of coronagraph observations.

Figure 7b shows the (ICME-removed) OMNI data at 1 AU as a function of longitude and time, highlighting the issue of locality of available observations. Applying the "corotation back" method yields the reconstruction of V

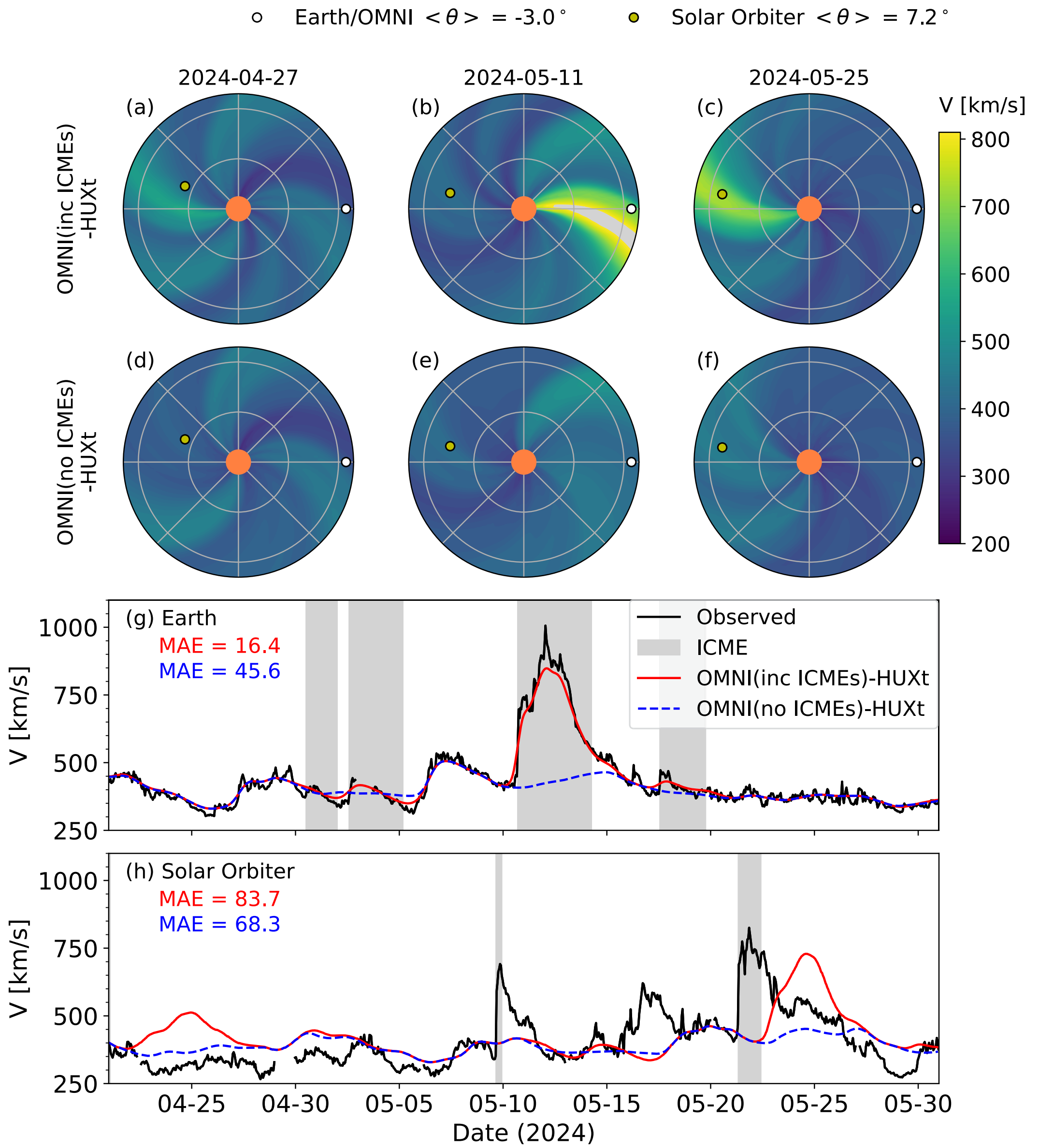

Figure 8. The importance of interplanetary CME (ICME) removal using the example of the observed and modeled solar wind at Earth and *Solar Orbiter* around the time of the May 2024 storms. Panels show: (a) to (c), the solar wind speed, V, in solar equatorial plane using the HUXt model constrained by OMNI observations backmapped to 0.1 AU, without the removal of ICMEs, for three different times. The location of Earth is shown by the white dot, *Solar Orbiter* by the yellow dot. (d) to (f) show the same, but with ICMEs removed from the OMNI data prior to backmapping. (g) V in near-Earth space observed by the OMNI spacecraft (black), reconstructed by HUXt constrained with OMNI without removal of ICMEs (red) and with ICMEs removed (blue-dashed). Intervals identified as ICMEs are shown as gray-shaded regions. (h) Same as g, but at the location of *Solar Orbiter*.

at all longitudes and times shown in Figure 7c. Corotation forward gives Figure 7d. This is identical to Figure 7c, but with a 27-day offset. Interpolation in time between corotation back and forward is shown in Figure 7e. Whilst the discontinuous jumps in solar wind speed every 27 days that result from the first two methods are removed, the resulting V structure is also smoothed out. Finally, application of the DTW method is shown in Figure 7f. This also removes the discontinuous V jumps of Panels (c) and (d), but retains more of the inherent stream structure. See (M. J. Owens & Nichols, 2021) for more detail.

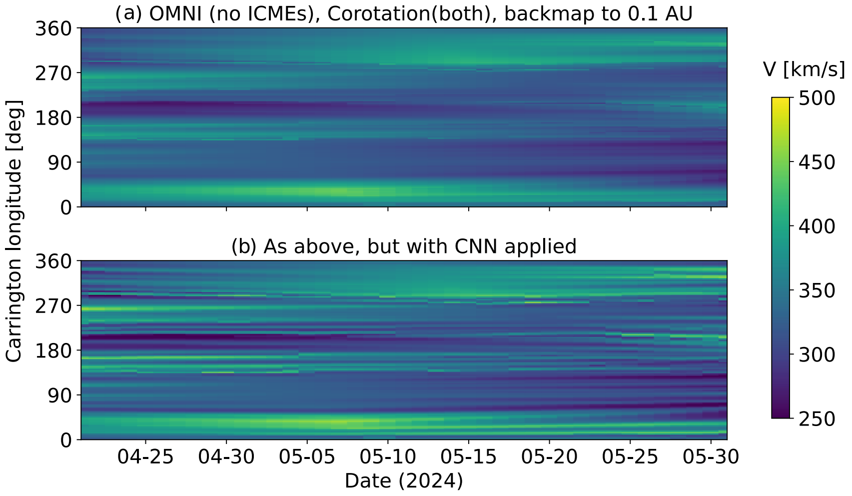

Figure 9. Example of the solar wind conditions at 0.1 AU, reconstructed around the time of the May 2024 storms. *V* is shown as a function of Carrington longitude and time. (a) interplanetary CMEs at AU are removed from the OMNI observations. Full longitudinal coverage at 1 AU is then obtained by corotating structures forward and backwards in time from the available OMNI observations (as shown in Figure 7e). The longitudinal profiles at 1 AU are then mapped back to 0.1 AU, accounting for the assumed acceleration profile. (b) Same as a, but the convolutional neural network is also applied to account for stream interactions between 0.1 and 1 AU.

Each longitudinal-reconstruction method shown in Figure 7c to f is individually backmapped, allowing for acceleration and longitudinal shift, and then run through the trained CNN to account for stream interaction. Figure 9a shows the result of backmapping the “corotation both” method to 0.1 AU before the CNN is applied. Figure 9b shows the additional step of applying the CNN. This does not change the large-scale stream structure, but sharpens the gradients at the stream boundaries, as shown in Figure 5. In both cases, the speeds are generally about 20% lower than the input ambient solar wind speeds at 1 AU.

The solar wind structure shown in Figure 9b is then used as the inner boundary condition to the HUXt model, to reconstruct the solar wind in the Earth's orbital plane out to 1 AU. The results of this OMNI-HUXt model are shown as the red lines in Figure 10g. By design, OMNI-HUXt provides a very good match to the ambient solar wind at Earth. The real test comes in the ability to reconstruct conditions at other heliospheric locations. Figure 10h shows the model solution and observations at *Solar Orbiter*, on the far side of the Sun, within 1 AU, and 10.2° separation from Earth in heliographic latitude. At *Solar Orbiter*'s location there is almost a 50% reduction in MAE from the new backmapping method compared to the standard WSA-HUXt solar wind reconstruction shown in Figure 2h. This suggests that the method may have great utility in dynamically mapping in situ solar observations back to the solar source surface in order to better understand their origin. However, there are two caveats to this. Firstly, this is only a single example period and a more thorough validation needs to be performed against observations over an extended period. Secondly, approach shown here is for post-hoc reconstruction; whereas the WSA-HUXt approach is primarily used for genuine forecasting.

With ICMEs removed from OMNI prior to backmapping, the intervals of transient ICMEs at Earth, particularly the storms in May 10-13, are obviously not captured. We reintroduce the CMEs as transient speed pulses at 0.1 AU (Odstrcil et al., 2004), using the cone-CME speeds, directions and timings estimated from coronagraph observations and listed in the DONKI catalog. For this period, there are 177 cone CMEs in the DONKI catalog, all of which are included in the model run, though most are not Earth or *Solar Orbiter* directed. For each CME we insert a solar wind speed perturbation at 0.1 AU with a fixed pulse duration of 8 hr (M. J. Owens et al., 2025). The resulting OMNI-Cone-HUXt solution, shown in blue, does capture the timing of the May storms at 1 AU very well, particularly the initial shock arrival time. The maximum *V* is in approximate agreement too, though the timing of the modeled and observed *V* maxima are about a day apart. Crucially, this transient treatment of CMEs means that false corotating streams are not created at other heliospheric locations, such as at *Solar Orbiter*.

At *Solar Orbiter*, the addition of cone CMEs produces approximately the right speed and timing for the 2025-5-22 ICME, but no cone CME was corresponds to the 2025-5-9 ICME. And a cone CME produces a transient fast

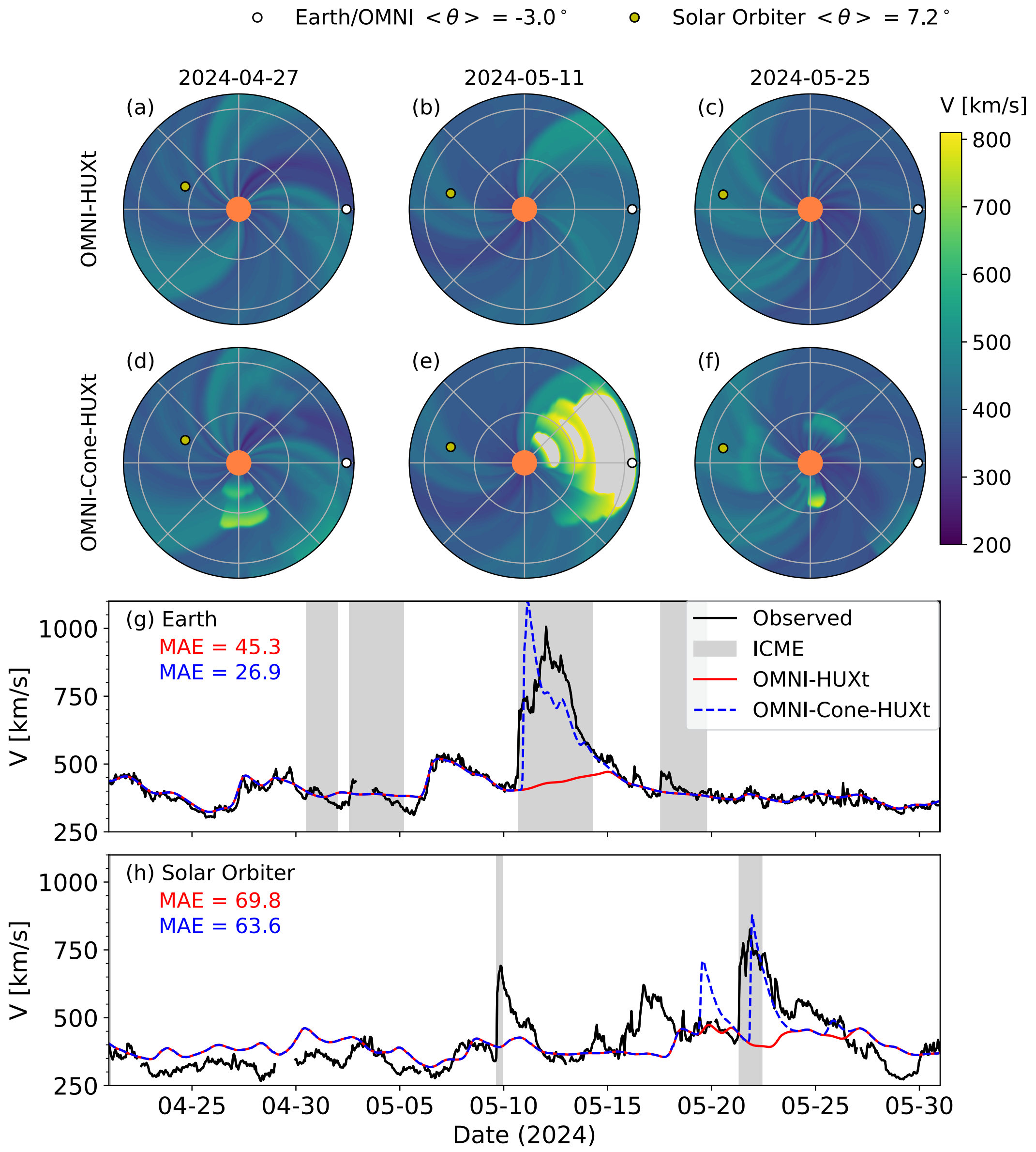

Figure 10. The results of OMNI-HUXt and OMNI-Cone-HUXt around the time of the May 2024 storms. Panels (a) to (c) show ambient V in the ecliptic plane at three times reconstructed from OMNI-HUXt. Earth is shown as a black circle. Panels (d) to (f) show the same as a to c, but for OMNI-Cone-HUXt. (g) Time series of V observed (black) in near-Earth space, with times of interplanetary CMEs shown as gray-shaded areas. The ambient OMNI-HUXt solution is shown in red, with solutions generated with the addition of cone-CMEs, OMNI-Cone-HUXt, shown by the blue-dashed line. (h) Same as g, but at the location of *Solar Orbiter*.

stream on 2025-5-20 with no corresponding ICME reported in the in situ data. This highlights the difficulty of accurately determining the near-Sun speed and direction of CMEs from coronagraph observations, particularly when only one viewpoint (near-Earth) is available.

Figure 10 summarizes the result from backmapping OMNI observations after using corotation forwards and backwards in time to construct full longitudinal coverage. But three other methods are used in Figure 7, namely corotation back in time, corotation forward in time, and DTW. Each of these can also be backmapped and serve as independent inner-boundary conditions to a solar wind model. And each of the four methods can additionally be used with and without cone-CME estimates. These eight solutions are shown in Figure 11 at both Earth and *Solar Orbiter* locations.

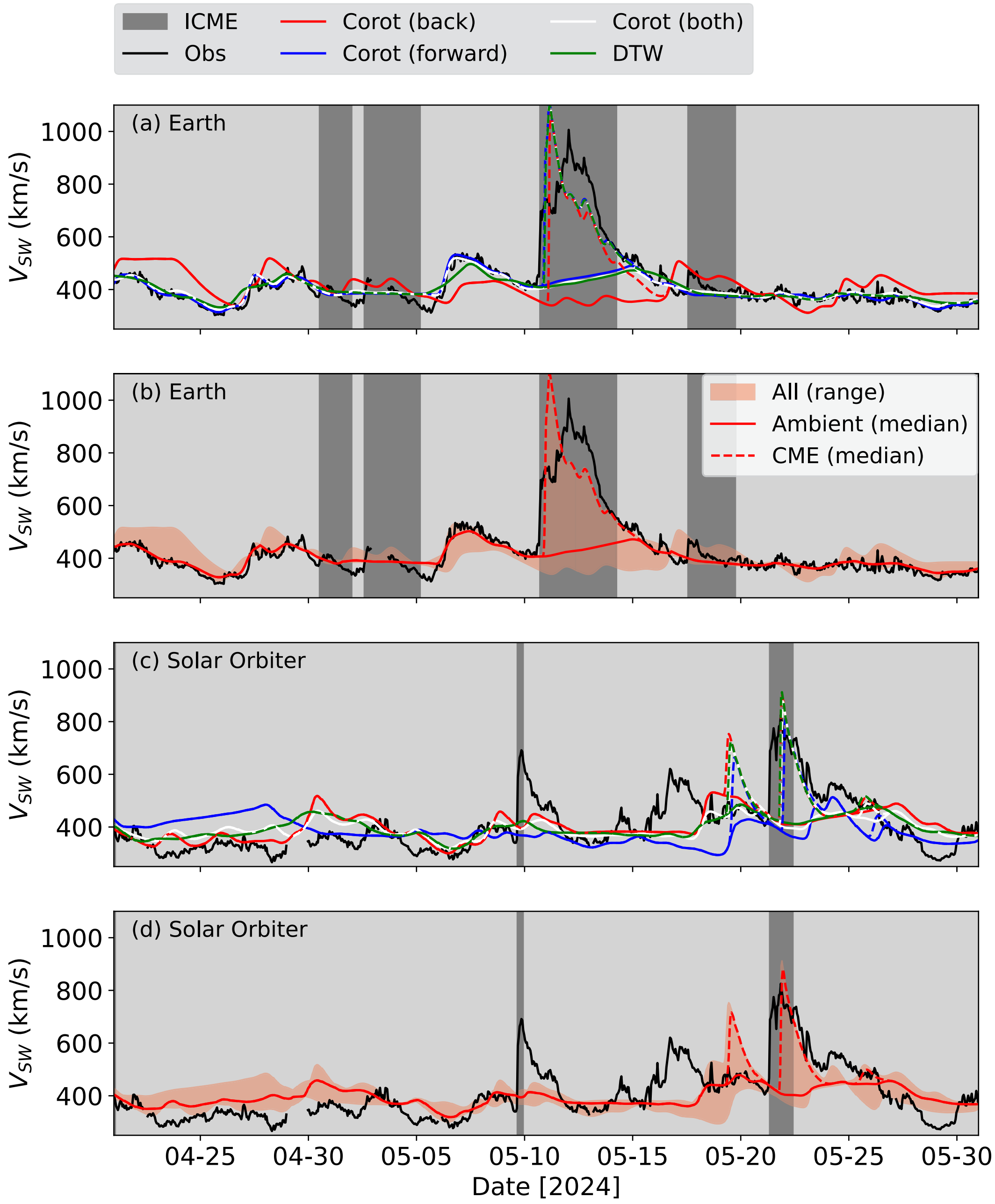

Figure 11. OMNI-HUXt solar wind solutions at Earth and *Solar Orbiter*. Observations are shown as the black line, with interplanetary CMEs shaded dark gray. (a) Individual model runs at Earth for different methods of longitudinal interpolation of the OMNI data, both with (solid) and without (dashed) the addition of cone coronal mass ejections. (b) Aggregations of these runs at Earth, with the solid red line showing the median value of all OMNI-HUXt runs, and the dashed red line the median of OMNI-Cone-HUXt runs. The red-shaded area shows full span of all runs. Panel (c) shows the same as (a), but at *Solar Orbiter*. Panel (d) shows the same as (b), but at *Solar Orbiter*.

It does not make physical sense to average together all eight solutions to produce a "most-likely" estimate; at times of fast ICMEs, averaging a cone-CME and an ambient solar wind run would produce intermediate speeds that are not consistent with any individual run. That is, the ensemble mean is not a member of the ensemble. Therefore we average the CME and non-CME model solutions separately. The full range of values is taken to be the maximum to minimum speeds across all eight model runs. Figure 11 shows the results.

At Earth, the ambient solar wind observations are generally within the ensemble spread. This is expected, as these same observations were backmapped to produce the HUXt inner-boundary conditions. At *Solar Orbiter*, there is reasonable agreement. But there is an extended interval of solar wind in late April through early May where the observed V is lower than the OMNI-HUXt ensemble. There are two potential explanations for this. It could be the large latitudinal difference between *Solar Orbiter* and Earth—approximately 10° at this time—means that *Solar Orbiter* is sampling very different ambient solar wind than the backmapped-OMNI data. This will almost certainly be a factor to some degree, and is likely to be of increasing importance near solar minimum, when the latitudinal gradients in V are high (M. J. Owens et al., 2020). A second possible explanation is that the acceleration profile used in HUXt—and hence in the backmapping process—is too weak. This has been suggested previously on the basis of inner-heliosphere observations (Bunting et al., 2024) and the timing of heliospheric current sheet encounters (Macneil et al., 2022) and will form the basis of a future study.

There is also an intermediate-speed ambient solar wind stream at *Solar Orbiter* on 17–18 May that is not captured by the OMNI-HUXt model. This is almost certainly a structure that exists at *Solar Orbiter*'s higher latitude that does not extend down to Earth. Indeed, Figure 2 shows evidence that the WSA-HUXt solution at *Solar Orbiter*'s latitude includes this structure, albeit with higher V than observed. This highlights the three-dimensional nature of the solar wind which can potentially be captured by models like WSA, and the limitation of backmapping in situ observations from a single latitude.

The largest deviations of observed V outside the range of the ensemble are at times of ICMEs. There are three different scenarios for such errors, all of which have examples in this period.

Firstly, there are "missed" ICMEs, as no cone CMEs were identified and inserted at 0.1 AU that correspond with the ICMEs subsequently seen in situ. At Earth, we see examples in the slow ICMEs on 1-5 May and later on the 17 May. Because these ICMEs are very close to the ambient solar wind speed, the model error is still small. A faster ICME with no cone-CME counterpart is seen at *Solar Orbiter* on 2024-5-10. Despite the short duration identified as ICME by Möstl et al. (2017), there is enhanced speed behind the ICME for approximately two days that is consequently missed by the model.

Secondly, there are "false alarm" ICMEs, where a cone CME has no ICME counterpart seen in situ. The only example in this interval is at *Solar Orbiter* on 2025-5-19. The ambient OMNI-HUXt reconstruction at this time agrees very well with the observed V. The fast ICME suggested by the OMNI-Cone-HUXt run is not observed, and this is unlikely to be a timing/speed error. The direction and/or angular width of the cone CME must have been in error, meaning it was incorrectly estimated to be directed at *Solar Orbiter*. Given the very high level of coronal activity during this period, such errors are perhaps not surprising.

Thirdly and finally, there are the cone-CMEs that are subsequently seen in situ as ICMEs, but the exact details of the modeled V profile differs from that observed. The examples of this are the very fast 11–13 May events at Earth, and the fast 22 May event at *Solar Orbiter*. In both cases, the timing and maximum V of the ICME is fairly well matched, though with the OMNI-Cone-HUXt values overestimating V in both cases (see also: M. J. Owens et al., 2025). Within the ICME itself, the small differences in the V profile are likely a result of the simple implementation by which CMEs are incorporated into the model. They are treated as pure V perturbations, with no internal magnetic structure (Odstrcil et al., 2004). This means that the internal dynamics, particularly expansion of CMEs (Agarwal & Mishra, 2024; Savani et al., 2009), will not be accurate. While more realistic modeling treatments of CMEs have been developed (e.g., Verbeke et al., 2019), it is not currently possible to fully determine the correct initial conditions on the basis of the available coronagraph observations.

5. Discussion

This study has outlined a methodology for using in situ solar wind observations, in particular from near-Earth space, to prescribe solar wind model inner-boundary conditions at 0.1 AU. The methodological framework is modular, meaning future developments which improve the solar wind acceleration profile, the removal of ICMEs, etc, can be readily integrated.

The central premise is that in situ observations of the ambient solar wind must be mapped back from 1 AU to 0.1 AU, accounting for three effects: (a) the continued solar wind acceleration out to 1 AU, (b) continued solar roation during solar wind transit, and (c) solar wind stream interactions during propagation to 1 AU. The first two aspects can be dealt with analytically, if an acceleration profile is assumed. The third is dealt with using a machine-learning approach trained on a large data set of synthetic solar wind solutions.

This method has been applied to the May 2024 interval, when a number of fast CMEs arrived at Earth in the form of transient ICMEs that generated significant geomagnetic activity. It is also a period when the *Solar Orbiter* spacecraft was on the far side of the Sun with respect to Earth, providing a useful test of how well near-Earth observations can be used to reconstruct solar wind conditions at other locations. Note that *Solar Orbiter* was more than 10° higher heliographic latitude than Earth at this time, so it also serves as a test of latitudinal separation. The discussion below relates to driving the HUXt solar wind model with OMNI data spanning the whole interval of interest. that is, we are reconstructing the solar wind structure after the fact, not testing a forecasting method. A future study will quantify the forecast potential of this method over a range of forecast lead times, solar-cycle conditions and spacecraft separations.

The fast ICMEs at Earth on 11–13 May demonstrate the need to remove transient structures from the solar wind observations at 1 AU before it is backmapped to the inner boundary at 0.1 AU. Failure to do so results in false corotating fast streams at other locations in the inner heliosphere. Using cone-CME estimates of CME speed and direction at 0.1 AU derived from coronagraph observations, it is then possible to reintroduce CMEs as true transient structures and reproduce the timing and speed of ICMEs at Earth. Additionally, this can capture non-Earth directed CMEs that were not present in the near-Earth data, that result in ICMEs at other heliospheric locations, such as at *Solar Orbiter*.

For the period considered, the solar wind structure reconstructed by this methodology—both at Earth and *Solar Orbiter*—is significantly more accurate than that determined by the standard "space-weather" approach of using a coronal model to provide the solar wind conditions at 0.1 AU. This suggests that the solar wind structure throughout the solar equatorial plane is well reconstructed, which will enable significantly improved mapping between in situ spacecraft observations and the solar source surface, as required by solar-connectivity science (e.g., Lyu et al., 2025; Yardley et al., 2024). It also presents an opportunity to investigate CME propagation through an accurate ambient solar wind structure. This is key to isolating the individual sources of uncertainty in CME arrival time forecasting (Kay et al., 2024; Riley et al., 2018; Wu et al., 2024).

There are, however, a number of caveats to this improved reconstruction and how it might generalize to other intervals and spacecraft configurations.

The May 2025 interval was around solar maximum, when the ambient solar wind structure is relatively simple (e.g., M. Owens, 2020). Slow ambient solar wind is prevalent at most latitudes, with a general absence of the fast coronal-hole wind that can reach down to equatorial regions at solar minimum. Thus, the sharp gradients in ambient solar wind structure with latitude are absent at solar maxmimum (M. J. Owens et al., 2020). We therefore expect the method presented here to suffer from greater inaccuracy with increasing latitudinal separation of source (e.g., Earth) and target (e.g., *Solar Orbiter*) latitudes at solar minimum. A future study will comprehensively characterize the performance of the backmapping reconstruction with solar cycle and latitude. Dealing with the solar-minimum solar wind structure will likely necessitate backmapping of in situ observations from multiple spacecraft at different heliolatitudes (e.g., OMNI and STEREO observations) and reconstructing latitudinal solar wind structure over the range sampled by ecliptic spacecraft. Better handling of the latitudinal structure of the solar wind is particularly important for providing solar wind information to support planetary observations (e.g., O'Donoghue et al., 2025).

It should also be stressed again that the method shown here was a post-hoc reconstruction, not a forecast, as it used in situ observations from both before and after the period of interest. In principle, the backmapping could be performed using only observations from the past, by assuming corotation back in time. For the ambient solar wind, this should produce results in very close agreement with the 27-day recurrence forecasts (Kohutova et al., 2016; M. J. Owens et al., 2013; Thomas et al., 2018). However, the backmapping approach would have the advantage that transient CMEs could be incorporated using the cone-CME estimates at 0.1 AU. By propagating CMEs though more accurate ambient solar wind, CME arrival time forecasting should improve (e.g., Case et al., 2008; Wu et al., 2024). Such a method of forecasting might also be desirable not just for potentially increased forecast accuracy, but also for forecast resilience; a forecast can be created without the need for photospheric magnetic field observations that underpin coronal models, should such data become unavailable.

Finally, we have proposed a simple ensemble of solar wind reconstructions that accounts for uncertainty in how single-spacecraft observations are extrapolated to provide full longitudinal coverage at a given time. For the May 2024 interval, the ensemble captures the ambient solar wind observed at *Solar Orbiter* for most of the time. There are two exceptions. Firstly, there is a fast ambient solar wind stream seen at *Solar Orbiter* that has no counterpart in the near-Earth observations. This is likely the result of different solar wind structures at Earth and *Solar Orbiter* latitudes. The second example is earlier in the period, when OMNI-HUXt systematically overestimates the solar wind speed at *Solar Orbiter* by around 100 km s^{-1}. This could also be the result of different solar wind structure at different latitudes. But it could also be due to the acceleration profile assumed by the HUXt model—and hence the backmapping procedure—being too weak (i.e., more acceleration takes place between 0.1 and 1 AU, meaning the true speeds close to the Sun are lower than assumed). This would be consistent with other findings (Bunting et al., 2024; Macneil et al., 2022). Consequently, the backmapping method provides a new means to probe the underlying acceleration profile, without having to rely on very rare radial alignments of spacecraft. This will form the basis of a future study.

Conflict of Interest

The authors declare no conflicts of interest relevant to this study.

Data Availability Statement

All code and data can be accessed in M. Owens (2025).

Acknowledgments
This work was part-funded by Science and Technology Facilities Council (STFC) Grant UKRI1207 and Natural Environment Research Council Grant NE/Y001052/1. CMJ's and MJR's work at DIAS was supported by Taighde Éireann–Research Ireland award 18/FRL/6199. This research made use of Astropy (Price-Whelan et al., 2018) and SunPy (Barnes et al., 2020) open source software packages for astronomy and solar physics. Figures for this article were made with Matplotlib (Hunter, 2007).

References

Agarwal, A., & Mishra, W. (2024). Non-conventional approach for deriving the radial sizes of coronal mass ejections at different instances: Discrepancies in the estimates between remote and in situ observations. *Monthly Notices of the Royal Astronomical Society*, *534*(3), 2458–2474. https://doi.org/10.1093/mnras/stae2260

Arge, C. N., Odstrcil, D., Pizzo, V. J., & Mayer, L. R. (2003). Improved method for specifying solar wind speed near the sun. *AIP Conference Proceedings*, Vol. 679(1), 190–193. https://doi.org/10.1063/1.1618574

Arnal, J. H., & Groth, C. P. T. (2024). Quantitative comparison of variational and sequential data assimilation techniques for one-dimensional initial-value problems of ideal MHD. *Computers and Fluids*, *282*, 106373. https://doi.org/10.1016/j.compfluid.2024.106373

Barnard, L., & Owens, M. (2022). HUXt—An open source, computationally efficient reduced-physics solar wind model, written in python. *Frontiers in Physics*, *10*, 1005621. https://doi.org/10.3389/fphy.2022.1005621

Barnes, W. T., Bobra, M. G., Christe, S. D., Freij, N., Hayes, L. A., Ireland, J., et al. (2020). The SunPy project: Open source development and status of the version 1.0 core package. *The Astrophysical Journal*, *890*(1), 68. https://doi.org/10.3847/1538-4357/ab4f7a

Bunting, K. A., Barnard, L., Owens, M. J., & Morgan, H. (2024). Constraints on solar wind density and velocity based on coronal tomography and parker solar probe measurements. *The Astrophysical Journal*, *961*(1), 64. https://doi.org/10.3847/1538-4357/ad1506

Case, A. W., Spence, H. E., Owens, M. J., Riley, P., & Odstrcil, D. (2008). Ambient solar wind's effect on ICME transit times. *Geophysical Research Letters*, *35*(15), L15105. https://doi.org/10.1029/2008GL034493

Hanlon, P. G., Dougherty, M. K., Forsyth, R. J., Owens, M. J., Hansen, K. C., Toth, G., et al. (2004). On the evolution of the solar wind between 1 and 5AU at the time of the Cassini-Jupiter flyby: Multi spacecraft observations of ICMEs including the formation of a merged interaction region. *Journal of Geophysical Research*, *109*(A9), A09S03. https://doi.org/10.1029/2003JA010112

Harvey, J. W., Hill, F., Hubbard, R. P., Kennedy, J. R., Leibacher, J. W., Pintar, J. A., et al. (1996). The global oscillation network group (GONG) project. *Science*, *272*(5266), 1284–1286. https://doi.org/10.1126/science.272.5266.1284

Hayakawa, H., Ebihara, Y., Mishev, A., Koldobskiy, S., Kusano, K., Bechet, S., et al. (2025). The solar and geomagnetic storms in 2024 May: A flash data report. *The Astrophysical Journal*, *979*(1), 49. https://doi.org/10.3847/1538-4357/ad9335

Heinemann, S. G., Pomoell, J., Caplan, R. M., Owens, M. J., Jones, S., Upton, L., et al. (2025). Quantifying uncertainties in solar wind forecasting due to incomplete solar magnetic field information. *The Astrophysical Journal*, *986*(2), 166. https://doi.org/10.3847/1538-4357/adcf9e

Hunter, J. D. (2007). Matplotlib: A 2D graphics environment. *Computing in Science & Engineering*, *9*(3), 90–95. https://doi.org/10.1109/MCSE.2007.55

Kay, C., Palmerio, E., Riley, P., Mays, M. L., Nieves-Chinchilla, T., Romano, M., et al. (2024). Updating measures of CME arrival time errors. *Space Weather*, *22*(7), e2024SW003951. https://doi.org/10.1029/2024SW003951

Keebler, T. (2021). MSWIM2D: Outer heliosphere solar wind dataset. [Presentation]. Online. Retrieved from https://whpi.hao.ucar.edu/showandtell/MSWIM2D/Keebler_WHPI.mp4

King, J. H., & Papitashvili, N. E. (2005). Solar wind spatial scales in and comparisons of hourly wind and ACE plasma and magnetic field data. *Journal of Geophysical Research*, *110*(A2), A02104. https://doi.org/10.1029/2004JA010649

Kohutova, P., Bocquet, F.-X., Henley, E. M., & Owens, M. J. (2016). Improving solar wind persistence forecasts: Removing transient space weather events, and using observations away from the sun-earth line. *Space Weather*, *14*(10), 802–818. https://doi.org/10.1002/2016SW001447

Lang, M., Browne, P., van Leeuwen, P. J., & Owens, M. (2017). Data assimilation in the solar wind: Challenges and first results. *Space Weather*, *15*(11), 1490–1510. https://doi.org/10.1002/2017SW001681

Lang, M., & Owens, M. J. (2019). A variational approach to data assimilation in the solar wind. *Space Weather*, *17*(1), 59–83. https://doi.org/10.1029/2018SW001857

Lang, M., Witherington, J., Turner, H., Owens, M. J., & Riley, P. (2021). Improving solar wind forecasting using data assimilation. *Space Weather*, *19*(7), e2020SW002698. https://doi.org/10.1029/2020SW002698

Lockwood, M., Owens, M. J., Brown, W., & Vázquez, M. (2025). The 2024 may event in the context of auroral activity over the past 375 yr. *Monthly Notices of the Royal Astronomical Society*, *540*(4), 3596–3624. https://doi.org/10.1093/mnras/staf827

Lyu, S., Wang, Y., & Owen, C. J. (2025). Connecting the Small Solar Wind Transients Observed Remotely to Their In Situ Measurement near 1 au. *The Astrophysical Journal*, *988*(2), 152. https://doi.org/10.3847/1538-4357/ade1d7

Macneil, A. R., Owens, M. J., Finley, A. J., & Matt, S. P. (2022). A statistical evaluation of ballistic backmapping for the slow solar wind: The interplay of solar wind acceleration and corotation. *Monthly Notices of the Royal Astronomical Society*, *509*(2), 2390–2403. https://doi.org/10.1093/mnras/stab2965

Majumdar, S., Reiss, M. A., Muglach, K., & Arge, C. N. (2025). What causes errors in wang–sheeley–arge solar wind modeling at L1? *The Astrophysical Journal*, *988*(2), 239. https://doi.org/10.3847/1538-4357/ade3d5

Merkin, V. G., Lyon, J. G., Lario, D., Arge, C. N., & Henney, C. J. (2016). Time-dependent magnetohydrodynamic simulations of the inner heliosphere. *Journal of Geophysical Research*, *121*(4), 2866–2890. https://doi.org/10.1002/2015JA022200

Möstl, C., Isavnin, A., Boakes, P. D., Kilpua, E. K. J., Davies, J. A., Harrison, R. A., et al. (2017). Modeling observations of solar coronal mass ejections with heliospheric imagers verified with the heliophysics system observatory. *Space Weather*, *15*(7), 955–970. https://doi.org/10.1002/2017SW001614

Muller, D., Marsden, R. G., St. Cyr, O. C., Gilbert, H. R., & Team, T. S. O. (2013). Solar orbiter. *Solar Physics*, *285*(1–2), 25–70. https://doi.org/10.1007/s11207-012-0085-7

O'Donoghue, J., Moore, L., Melin, H., Stallard, T., Kurth, W. S., Owens, M., et al. (2025). Sub-auroral heating at Jupiter following a solar wind compression. *Geophysical Research Letters*, *52*(7), e2024GL113751. https://doi.org/10.1029/2024GL113751

Odstrcil, D., Riley, P., & Zhao, X.-P. (2004). Numerical simulation of the 12 may 1997 interplanetary CME event. *Journal of Geophysical Research*, *109*(A2), A02116. https://doi.org/10.1029/2003JA010135

Owen, C. J., Bruno, R., Livi, S., Louarn, P., Janabi, K. A., Allegrini, F., et al. (2020). The solar orbiter solar wind analyser (SWA) suite. *Astronomy and Astrophysics*, *642*, A16. https://doi.org/10.1051/0004-6361/201937259

Owens, M. (2020). Solar-wind structure. *Oxford Research Encyclopedia of Physics*. https://doi.org/10.1093/acrefore/9780190871994.013.19

Owens, M. (2025). University-of-Reading-Space-Science/HUXt_insitu: Accepted article release. *Zenodo*. https://doi.org/10.5281/zenodo.17672607

Owens, M., Lang, M., Barnard, L., Riley, P., Ben-Nun, M., Scott, C. J., et al. (2020a). A computationally efficient, time-dependent model of the solar wind for use as a surrogate to three-dimensional numerical magnetohydrodynamic simulations. *Solar Physics*, *295*(3), 43. https://doi.org/10.1007/s11207-020-01605-3

Owens, M., Riley, P., Lang, M., & Lockwood, M. (2019). Near-earth solar wind forecasting using corotation from L5: The error introduced by heliographic latitude offset. *Space Weather*, *17*(7), 1105–1113. https://doi.org/10.1029/2019SW002204

Owens, M. J., Barnard, L. A., Verbeke, C., McGinness, B. P. S., Turner, H., Chi, Y., et al. (2025). Implications of using spheroidal "Cone Model" CMEs in solar-wind models. *Space Weather*, *23*(6), e2025SW004397. https://doi.org/10.1029/2025SW004397

Owens, M. J., Chakraborty, N., Turner, H., Lang, M., Riley, P., Lockwood, M., et al. (2022). Rate of change of large-scale solar-wind structure. *Solar Physics*, *297*(7), 83. https://doi.org/10.1007/s11207-022-02006-4

Owens, M. J., Challen, R., Methven, J., Henley, E., & Jackson, D. R. (2013). A 27 day persistence model of near-Earth solar wind conditions: A long lead-time forecast and a benchmark for dynamical models. *Space Weather*, *11*(5), 225–236. https://doi.org/10.1002/swe.20040

Owens, M. J., Lang, M., Riley, P., Lockwood, M., & Lawless, A. S. (2020b). Quantifying the latitudinal representivity of in situ solar wind observations. *Journal of Space Weather and Space Climate*, *10*, 8. https://doi.org/10.1051/swsc/2020009

Owens, M. J., & Nichols, J. D. (2021). Using in situ solar-wind observations to generate inner-boundary conditions to outer-heliosphere simulations – I. Dynamic time warping applied to synthetic observations. *Monthly Notices of the Royal Astronomical Society*, *508*(2), 2575–2582. https://doi.org/10.1093/mnras/stab2512

Owens, M. J., Riley, P., & Horbury, T. S. (2017). Probabilistic solar wind and geomagnetic forecasting using an analogue ensemble or "Similar Day" approach. *Solar Physics*, *292*(5), 69. https://doi.org/10.1007/s11207-017-1090-7

Palmerio, E., Maharana, A., Lynch, B. J., Scolini, C., Good, S. W., Pomoell, J., et al. (2023). Modeling a coronal mass ejection from an extended filament channel. II. Interplanetary propagation to 1 au. Astrophys. *The Journal*, *958*(1), 91. https://doi.org/10.3847/1538-4357/ad0229

Paszke, A., Gross, S., Massa, F., Lerer, A., Bradbury, J., Chanan, G., et al. (2019). PyTorch: An imperative style, high-performance deep learning library. In *Proceedings of the 33rd international conference on neural information processing systems* (pp. 8026–8037). Curran Associates Inc.

Pizzo, V. J. (1991). The evolution of corotating stream fronts near the ecliptic plane in the inner solar system. II - Three-Dimensional tilted-dipole fronts. *Journal of Geophysical Research*, *96*, 5405–5420. https://doi.org/10.1029/91JA00155

Pomoell, J., & Poedts, S. (2018). EUHFORIA: European heliospheric forecasting information asset. *Journal of Space Weather and Space Climate*, *8*, A35. https://doi.org/10.1051/swsc/2018020

Price-Whelan, A. M., Sipőcz, B. M., Günther, H. M., Lim, P. L., Crawford, S. M., Conseil, S., et al. (2018). The astropy project: Building an open-science project and status of the v2. 0 core package. *The Astronomical Journal*, *156*(3), 123. https://doi.org/10.3847/1538-3881/aabc4f

Richardson, I. G., & Cane, H. V. (2010). Near-Earth interplanetary coronal mass ejections during solar cycle 23 (1996 – 2009): Catalog and summary of properties. *Solar Physics*, *264*(1), 189–237. https://doi.org/10.1007/s11207-010-9568-6

Riley, P., Ben Nun, M., Linker, J., Owens, M. J., & Horbury, T. S. (2017). Forecasting the properties of the solar wind using simple pattern recognition. *Space Weather*, *15*(3), 526–540. https://doi.org/10.1002/2016SW001589

Riley, P., Linker, J. A., & Arge, C. N. (2015). On the role played by magnetic expansion factor in the prediction of solar wind speed. *Space Weather*, *13*(3), 154–169. https://doi.org/10.1002/2014SW001144

Riley, P., Linker, J. A., & Mikic, Z. (2001). An empirically-driven global MHD model of the solar Corona and inner heliosphere. *Journal of Geophysical Research*, *106*, 15889–15902. https://doi.org/10.1029/2000JA000121

Riley, P., & Lionello, R. (2011). Mapping solar wind streams from the sun to 1 AU: A comparison of techniques. *Solar Physics*, *270*(2), 575–592. https://doi.org/10.1007/s11207-011-9766-x

Riley, P., Mays, L., Andries, J., Amerstorfer, T., Biesecker A, D., Delouille, V., et al. (2018). Forecasting the arrival time of coronal mass ejections: Analysis of the CCMC CME scoreboard. *Space Weather*, *16*(9), 1245–1260. https://doi.org/10.1029/2018SW001962

Samara, E., Arge, C. N., Pinto, R. F., Magdalenić, J., Wijsen, N., Stevens, M. L., et al. (2024). Calibrating the WSA model in EUHFORIA based on parker solar probe observations. *The Astrophysical Journal*, *971*(1), 83. https://doi.org/10.3847/1538-4357/ad53c6

Savani, N., Rouillard, A. P., Davies, J. A., Owens, M. J., Forsyth, R. J., Davis, C. J., & Harrison, R. A. (2009). The radial width of a coronal mass ejection between 0.1 and 0.4 AU estimated from the heliospheric imager on STEREO. *Ann. Geophys.*, *27*(11), 4349–4358. https://doi.org/10.5194/angeo-27-4349-2009

Tao, C., Kataoka, R., Fukunishi, H., Takahashi, Y., & Yokoyama, T. (2005). Magnetic field variations in the Jovian magnetotail induced by solar wind dynamic pressure enhancements. *Journal of Geophysical Research*, *110*(A11), A11208. https://doi.org/10.1029/2004JA010959

Thomas, S. R., Fazakerley, A., Wicks, R. T., & Green, L. (2018). Evaluating the skill of forecasts of the near-earth solar wind using a space weather monitor at L5. *Space Weather*, *16*(7), 814–828. https://doi.org/10.1029/2018SW001821

Toth, G., Sokolov, I. V., Gombosi, T. I., Chesney, D. R., Clauer, C. R., De Zeeuw, D. L., et al. (2005). Space weather modeling framework: A new tool for the space science community. *Journal of Geophysical Research*, *110*(A12), A12226. https://doi.org/10.1029/2005JA011126

Turner, H., Lang, M., Owens, M., Smith, A., Riley, P., Marsh, M., & Gonzi, S. (2023). Solar wind data assimilation in an operational context: Use of near-real-time data and the forecast value of an L5 monitor. *Space Weather*, *21*(5), e2023SW003457. https://doi.org/10.1029/2023SW003457

Turner, H., Owens, M., Lang, M., & Gonzi, S. (2021). The influence of spacecraft latitudinal offset on the accuracy of corotation forecasts. *Space Weather*, *19*(8), e2021SW002802. https://doi.org/10.1029/2021SW002802

van der Holst, B., Sokolov, I. V., Meng, X., Jin, M. W. B., Manchester, I., Tóth, G., & Gombosi, T. I. (2014). ALFVÉN WAVE SOLAR MODEL (AWSoM): Coronal HEATING. *The Astrophysical Journal*, *782*(2), 81. https://doi.org/10.1088/0004-637X/782/2/81

Verbeke, C., Pomoell, J., & Poedts, S. (2019). The evolution of coronal mass ejections in the inner heliosphere: Implementing the spheromak model with EUHFORIA. *Astron. & Astrophys.*, *627*, A111. https://doi.org/10.1051/0004-6361/201834702

Wang, Y.-M., & Sheeley, J. N. R. (1990). Solar wind speed and coronal flux-tube expansion. *The Astrophysical Journal*, *355*, 726. https://doi.org/10.1086/168805

Watson, S., Scott, C., Owens, M., Barnard, L., & Lang, M. (2025). Statistical analysis of comet disconnection events using STEREO HI and a data-assimilative solar wind model. *The Astrophysical Journal*, *982*(2), 66. https://doi.org/10.3847/1538-4357/adb978

Wu, C.-C., Liou, K., Wood, B. E., & Hutting, L. (2024). Effects of background solar wind and drag force on the propagation of coronal-mass-ejection-driven shocks. *The Astrophysical Journal*, *977*(2), 212. https://doi.org/10.3847/1538-4357/ad88ee

Yardley, S. L., Brooks, D. H., D'Amicis, R., Owen, C. J., Long, D. M., Baker, D., et al. (2024). Multi-source connectivity as the driver of solar wind variability in the heliosphere. *Nature Astronomy*, *8*(8), 953–963. https://doi.org/10.1038/s41550-024-02278-9

Zhao, X. P. (2008). Inversion solutions of the elliptic cone model for disk frontside full halo coronal mass ejections. *Journal of Geophysical Research*, *113*(A2), 2101. https://doi.org/10.1029/2007JA012582